Passband Tunable Reconfigurable Frequency Selective Surface With Wide Tuning Range

Lin-Man Zhang, *Graduate Student Member, IEEE*, Xiao Ding, *Senior Member*, *IEEE*, and Maurizio Bozzi, *Fellow, IEEE*

***Abstract*—In this paper, a transmission passband tunable reconfigurable frequency selective surface (RFSS) with a wide tuning range is proposed. First, the design guidelines of a wide tuning range for RFSS embedded with varactors are deduced based on the equivalent circuit model (ECM) method. An ECM with passband wide range tunability is proposed. Second, a paradigm is designed based on the proposed ECM and the design guidelines. The proposed RFSS unit can provide a series of tunable transmission passbands from 1.51 to 4.96 GHz (with a relative bandwidth of 106.6%) by embedded voltage-driven varactors and PIN diodes. Meanwhile, the transmission passbands can maintain high transmittance (insertion loss fluctuates between 0.35 and 2.55 dB). In addition, taking full advantage of the tunability of RFSS, the proposed unit can maintain the resonant frequencies and insertion loss stable when the incident angle varies from 0° to 70° from the simulated results. Finally, the prototype is fabricated and measured. The measurement and simulation results are in good agreement. The excellent properties of the proposed unit verify the effectiveness and feasibility of the proposed design method. This paper provides a practical scheme to broaden the passband tunable range and the application scenarios of RFSS.**

***Index Terms*—Passband tunability, reconfigurable frequency selective surface (RFSS), varactor embedded, wide tuning range**

I. Introduction

FREQUENCY selective surface (FSS) is a two-dimensional periodic planar structure described by a unit cell containing either metallic patches or apertures and thin dielectric slabs [1]. It has been put forward to apply in many areas due to its ability to manipulate electromagnetic (EM) waves. One of the most important and typical applications is band-pass FSS designed as radomes [2]. With the deeper research on FSS and the expansion of its application areas, researchers have developed a wide variety of FSS to achieve more novel properties [3], [4], [5], [6], [7]. A great number of novel features of FSS have been realized by loading resistors, capacitors, and other elements on the FSS, such as miniaturization, tunable transmission passband, polarization selection, etc. For example, by embedding resistors, EM wave absorption properties are realized [8], [9], [10], [11], [12]. By embedding capacitors, the miniaturization of FSS is realized [13], [14], [15], [16], [17]. Meanwhile, the research on bandpass FSS has become more popular [18], [19], [20].

Under the conditions of highly intelligent integration of various devices, the reconfigurable frequency selective surface (RFSS) embedded with active elements (varactor and PIN diode, etc.) has emerged [21], [22], [23]. The RFSS offers significant advantages in terms of flexibility after fabrication. For example, a varactor-tunable bandpass RFSS is proposed in [13]. By adjusting the supplied voltage of the varactor, the transmission passband of the proposed RFSS can be tuned from 3.7 to 5.2 GHz with a relative bandwidth (RBW) of 33.7% and the insertion loss (IL) between 3 and 6 dB. In [14], a dual-band RFSS with high selectivity and independently switchable characteristics is proposed. By the voltage-driven PIN diodes, the two transmission passbands at 3.03 and 4.33 GHz with the corresponding ILs are 0.44 and 1.06 dB can be switched on or off independently. Among them, the transmission passband tunable RFSS embedded with varactor has been widely studied and expanded due to its ease of electrical control and functional applications [24], [25], [26], [27], [28], [29], [30], [31], [32], [33], [34] [35].

Due to the exponentially growing demand for the vast amount of wireless data volumes, the whole communication system is faced with challenges in channel capacity, interference, stealth performance, and so on. Antennas are gradually developing into multi-band antenna, broadband antenna, wideband antenna, and so on. This places new demands on the FSS radome used in conjunction with it. The transmission passband tunable RFSS with a wide range can increase the channel capacity through reconfigurable passbands, minimize interference or eavesdropping on unexpected sources by continuous frequency hopping operation, and improve the stealth capability of aircraft. Therefore, the high-performance wide range passband tunable RFSS can broaden the application scenarios of wideband or multi-band antennas.

However, due to the limited performance of the active elements and the difficulty of the unit design, the contradiction between passband tunability and IL is difficult to balance. A three-dimensional tunable bandpass FSS with a wide tuning range is presented in [26]. The passband can be tuned from 1.4 to 2.75 GHz with an IL of 4.5 – 1.0 dB. There is room for improvement in both the tunable range and IL of this work. In [30], a square-slot FSS loaded with varactors aimed to achieve a high-transmittance varactor-tunable is proposed. It can offer a series of transmission passbands when the bias voltage applied

Manuscript received 27 October 2023. This work was supported in part by the National Natural Science Foundation of China under Grant 62171093. *(Corresponding author: Xiao Ding)*

L. -M. Zhang, X. Ding are with the Institute of Applied Physics, University of Electronic Science and Technology of China, Chengdu 610054, China. (e-mail: linmanzhang@std.uestc.edu.cn; xding@uestc.edu.cn).

Maurizio Bozzi is with the Department of Electrical, Computer and Biomedical Engineering, University of Pavia, 27100 Pavia, Italy. (e-mail: maurizio.bozzi@unipv.it).

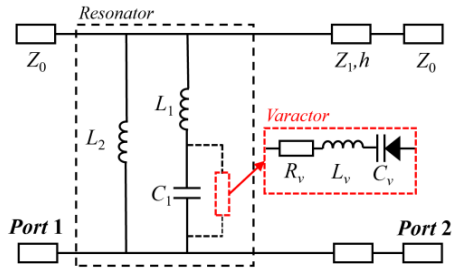

Fig. 1. The ECM of transmission passband tunable RFSS with varactor embedded.

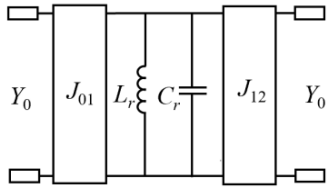

Fig. 2. The generalized bandpass circuit of the proposed ECM using *J*-inverters.

to the varactors is tuned from 5 to 20 V with an IL of 1.09 dB maximum. However, the passband tunable RBW is only 19.7% (from 4.84 to 5.9 GHz). How to fully utilize the performance of the active element itself to achieve a wider passband tunable range and a lower passband IL is what all researchers are committed to.

This paper is devoted to widening the transmission passband tunable range of RFSSs embedded with active elements. First, we establish a typical equivalent circuit model (ECM) of typical bandpass RFSS. Then, design guidelines for wide-range passband tunable RFSS are obtained by analyzing the variables that affect the tuning bandwidth and the relationships between them. Based on the proposed method and guidelines, we design a wide tuning range ECM. Through the rational utilization of active elements and the design of the RFSS configuration, an RFSS unit with a wide tuning range and low IL is proposed. The structure, active elements and parameters determination of the paradigm follows the theoretical guidelines, which validate the feasibility and rationality of the proposed method. This paper provides a viable approach to solve the contradiction between the tuning range and IL for tunable RFSS embedded with varactors.

This article is organized as follows. In Section II, by analyzing the ECM of the typical varactor-based RFSS, the general working mechanism of the tunable RFSS and the influence of the tunable variables on the transmission performances are obtained. More importantly, the wide tunable range guidelines and ECM are obtained. A paradigm with a wide transmission passband tuning range and high transmittance is proposed in Section III. This section demonstrates its operating mechanism and excellent simulation and measurement performances. Section IV provides the concluding remarks.

II. Analysis and Design Method

The ECM of the typical transmission passband tunable RFSS embedded with varactors is shown in Fig. 1, which can be equivalent to L_1 and C_1 in series and then L_2 in parallel [36]. The varactors embedded in the unit to adjust the transmission passband are connected in parallel to the equivalent capacitor C_1. The equivalent circuit of the varactor is shown in the blue block of Fig. 1, which can be expressed as R_v, L_v, and C_v in series (parasitic capacitance is contained in C_v).

A. The ECM Analysis of RFSS With Varactors

From the ECM approach, the [*ABCD*] in Fig. 1 can be expressed as a cascading of the matrices [37],

$$\begin{bmatrix} A & B \\ C & D \end{bmatrix} = M_{res} \cdot M_s = \begin{bmatrix} 1 & 0 \\ Y_{res} & 1 \end{bmatrix} \begin{bmatrix} \cos\phi & jZ_1 \sin\phi \\ j\dfrac{\sin\phi}{Z_1} & \cos\phi \end{bmatrix} \quad (1)$$

When irradiated by TE wave,

$$\phi = \frac{\omega h}{c}\sqrt{\varepsilon_d - \sin^2\theta} \text{ and } Z_1 = Z_0 / \sqrt{\varepsilon_d - \sin^2\theta}\,. \quad (2)$$

When irradiated by TM wave,

$$\phi = \frac{\omega h \varepsilon_r}{c\sqrt{\varepsilon_d - \sin^2\theta}} \text{ and } Z_1 = Z_0\sqrt{\varepsilon_d - \sin^2\theta}/\varepsilon_d\,. \quad (3)$$

in which, θ is the incidence angle of the EM wave. h is the height of the substrate. $\varepsilon_d = \varepsilon_r(1 - j\tan\delta)$, in which, ε_r and $\tan\delta$ are the relative dielectric permittivity and loss tangent of the dielectric substrate, respectively. Z_0 and Z_1 represent the wave impedances of free space and substrate, respectively. $Z_0 = 120\pi$ and $Z_1 = Z_0/\sqrt{\varepsilon_d}$. In (1), the Y_{res} is the admittance of the *Resonator* and can be expressed as:

$$Y_{res} = \frac{Y_N}{Y_D} \quad (4)$$

$$\begin{aligned} Y_N = {} & 1 + j\omega C_v R_v - \omega^2\left[(L_1 + L_2)(C_1 + C_v) + L_v C_v\right] \\ & - j\omega^3 (L_1 + L_2) C_v C_1 R_v + \omega^4 (L_1 + L_2) L_v C_v C_1 \end{aligned} \quad (5)$$

$$Y_D = j\omega L_2 \begin{Bmatrix} 1 + j\omega C_v R_v - \omega^2\left[L_1(C_1 + C_v) + L_v C_v\right] \\ -j\omega^3 L_1 C_1 C_v R_v + \omega^4 L_1 L_v C_v C_1 \end{Bmatrix}. \quad (6)$$

Simplifying (5) and (6) according to the magnitude of the variables, then

$$Y_N \approx 1 - \omega^2\left[(L_1 + L_2)(C_1 + C_v) + L_v C_v\right] + j\omega C_v R_v \quad (7)$$

$$Y_D \approx j\omega L_2\left\{1 + j\omega C_v R_v - \omega^2\left[L_1(C_1 + C_v) + L_v C_v\right]\right\}. \quad (8)$$

Let $Y_N = 0$, solving for ω yields the transmission pole f_p:

$$f_p = 1/2\pi\sqrt{(L_1 + L_2)(C_1 + C_v) + L_v C_v}\,. \quad (9)$$

From (8), there is a transmission zero f_z at:

$$f_z = 1/2\pi\sqrt{L_1(C_1 + C_v) + L_v C_v}\,. \quad (10)$$

The corresponding generalized bandpass circuit using *J*-inverters is provided in Fig. 2. Then, we can get [38]:

$$C_r = \frac{\left[L_2(C_1 + C_v) + L_v C_v\right]^2}{L_2^2(C_1 + C_v)} \quad (11)$$

$$\Delta f = \frac{J_{01}^{\ 2} \cdot g_0 \cdot g_1}{2\pi \cdot C_r \cdot Y_0} = \frac{J_{12}^{\ 2} \cdot g_1 \cdot g_2}{2\pi \cdot C_r \cdot Y_0} \tag{12}$$

where $J_{01} = J_{12} = Y_0$, g_0, g_1, and g_2 are the prototype values of the lowpass filter. There is $g_0 = g_2$ for one-order filter. Δf is the 3-dB bandwidth of the passband. For this ECM, the only variable in the tuning process is C_v. From (11), derive C_r concerning C_v:

$$\frac{\partial C_r}{\partial C_v} = \frac{L_1\left(L_1 + 2L_v\right)}{L_2^{\ 2}} + \frac{L_v^{\ 2} C_v \left(2C_1 + C_v\right)}{L_2^{\ 2}\left(C_1 + C_v\right)^2} > 0 \tag{13}$$

C_r is proportional to C_v. Therefore, the 3-dB bandwidth of the passband is inversely proportional to C_r. As the varactor diode capacitance C_v decreases, C_r decreases, and the bandwidth increases. That is, the bandwidth of the passband necessarily increases with the resonant frequency.

Among the parameters of the varactor, besides C_v, L_v also affects the resonant pole of the RFSS. Due to R_v cannot be 0, the $\mathrm{Im}\{Y_N\}$ must be greater than 0. The smaller R_v, the smaller $\mathrm{Im}\{Y_N\}$, the higher the resonant level at the f_p, and finally, the smaller the IL.

In addition, from (2) and (3), the loss tangent tanδ of the dielectric substrate is directly proportional to the IL at the transmission passband. If the dielectric substrate thickness h is small enough ($h < 0.1\lambda$), the tanδ of the low-loss dielectric substrate has a negligible effect on the transmission performance.

Once the varactor is selected, the active parameters of L_v and C_v are fixed. According to (9) and (10), we can obtain the initial solutions of L_1, C_1, and L_2 from the desired f_p and f_z. However, the circuit parameters of the ECM are highly closely related to the structure of the FSS. The determination of equivalent circuit parameters needs to be integrated with the unit design.

B. The Tuning Range Analysis

We define the tuning range of the varactor capacitance C_v to be adjustable from C_{vL} to C_{vH} as the bias voltage decreases. From (9), the corresponding resonant frequency of the transmission passband f_p can be varied from f_H to f_L with $C_v = C_{vL}$ to $C_v = C_{vH}$. Then, the RBW of the transmission passband tunable RFSS is:

$$RBW = \frac{2\left(f_H - f_L\right)}{f_H + f_L} = \frac{2\left[\alpha + 2\,{C_1}/{C_{vL}} + 1 - 2\sqrt{\left(1 + {C_1}/{C_{vL}}\right)\left(\alpha + {C_1}/{C_{vL}}\right)}\right]}{\alpha - 1} \tag{14}$$

where α is the capacitance tuning ratio of the varactor and $\alpha = C_{vH}/C_{vL}$.

From (14), the RBW of the transmission passband is related to the RFSS structural capacitance C_1, the lower limit C_{vL}, and the capacitance tuning ratio of the varactor α.

Derive (14) concerning C_1, we can get:

$$\frac{\partial RBW}{\partial C_1} = \frac{4}{C_{vL}\left(\alpha - 1\right)}\left[1 - \frac{2C_1 + \alpha C_{vL} + C_{vL}}{2\sqrt{\left(C_{vL} + C_1\right)\left(\alpha C_{vL} + C_1\right)}}\right] \le 0 \tag{15}$$

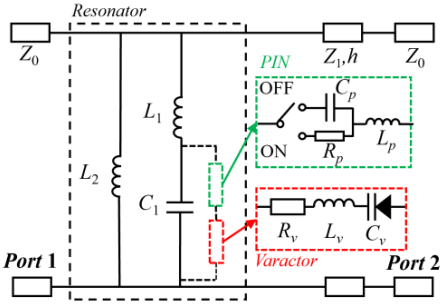

Fig. 3. The proposed ECM with a wide tuning range.

From (15), the RBW is monotonically decreasing concerning C_1, i.e., RBW gets the maximum value when C_1 takes the minimum value.

Derive (14) concerning α, we can get:

$$\frac{\partial RBW}{\partial \alpha} = \frac{2\sqrt{1 + \frac{C_1}{C_{vL}}}\left[1 + \frac{2C_1}{C_{vL}} + \alpha - 2\sqrt{1 + \frac{C_1}{C_{vL}}}\sqrt{\alpha + \frac{C_1}{C_{vL}}}\right]}{\left(\alpha - 1\right)^2} \ge 0 \tag{16}$$

From (16), the RBW is monotonically increasing about α. The larger α is, the larger RBW can be achieved.

Derive (14) concerning C_{vL}, we can get:

$$\frac{\partial RBW}{\partial C_{vL}} = \frac{-2C_1\left[2\sqrt{\left(\alpha + \frac{C_1}{C_{vL}}\right)\left(1 + \frac{C_1}{C_{vL}}\right)} + \alpha + 1 + \frac{2C_1}{C_{vL}}\right]}{\left(\alpha - 1\right)C_{vL}^2} \le 0 \tag{17}$$

From (17), the RBW is monotonically decreasing concerning C_{vL}. The smaller C_{vL} is, the larger the RBW can be.

From the above analysis, we can conclude that the RFSS with embedded varactors, expecting to obtain a larger transmission passband tunable RBW needs to follow:

1) C_1 should be as small as possible;
2) The capacitance tuning range of the varactor α should be as large as possible.
3) The lower limit of the varactor C_{vL} should be as small as possible.

In addition, L_1 and L_2 are independent of the passband tunable RBW, which can be exploited to design for other properties. For RFSS, we can achieve excellent performance by designing the structure or selecting the active elements to realize the desired equivalent circuit parameters. The following paradigm in Section III is provided to demonstrate the design method and to verify the conclusions.

C. The Proposed ECM With Wide Tuning Range

Fig. 3 proposed an ECM with a wide tuning range based on the above analysis. In order to obtain a wide tunable range, the following methods have been adopted:

1) Reduce C_1;
2) Expand the tuning range α by connecting a PIN in series;
3) Select the varactor model with the small lower limit C_{vL}.

The C_1 is related to the center patch [39]. We can reduce C_1 by decreasing the patch area, changing the patch pattern, etc. The PIN introduced in the proposed ECM can be equated to a

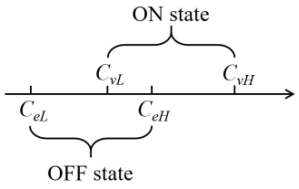

Fig. 4. The capacitance tuning range when the PIN is in different states.

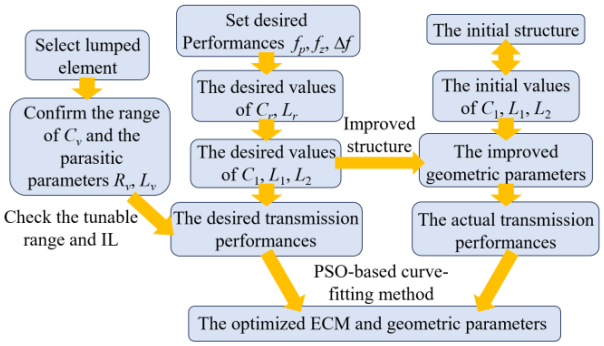

Fig. 5. The design flow of the proposed method.

small resistor R_p in series with the package inductor L_p in the ON state and a small capacitor C_p in series with the package inductor L_p in the OFF state.

When the PIN is in the ON state, the Y_{res} can be expressed as:

$$Y_{res}=\frac{1-\omega^2\left[\left(L_1+L_2\right)\left(C_1+C_v\right)+\left(L_v+L_p\right)C_v\right]+j\omega C_v\left(R_v+R_p\right)}{j\omega L_2\left\{1+j\omega C_v\left(R_v+R_p\right)-\omega^2\left[L_1\left(C_1+C_v\right)+\left(L_v+L_p\right)C_v\right]\right\}}. \tag{18}$$

Compared to the ECM without PINs (as shown in Fig. 1), the main effect is that the package inductance and resistance of active element changes from that of the varactor (L_v, R_v) to its series connection with the PIN (L_v + L_p, R_v + R_p). From the above, it is clear that the package inductance has almost no effect on the tuning range. The package resistance affects the IL at the transmission passband.

When the PIN is in the OFF state, the Y_{res} can be expressed as:

$$Y_{res}=\frac{1-\omega^2\left[\left(L_1+L_2\right)\left(C_1+C_e\right)+\left(L_v+L_p\right)C_e\right]+j\omega C_e R_v}{j\omega L_2\left\{1+j\omega C_e R_v-\omega^2\left[L_1\left(C_1+C_e\right)+\left(L_v+L_p\right)C_e\right]\right\}} \tag{19}$$

where

$$C_e=\frac{C_vC_p}{C_v+C_p}. \tag{20}$$

As the varactor capacitance changes, there is:

$$C_{eL}=\frac{C_{vL}C_p}{C_{vL}+C_p}<C_{eH}=\frac{C_{vH}C_p}{C_{vH}+C_p}. \tag{21}$$

When the PIN is in the different state, there are:

$$C_{eL}<C_{vL}<C_{vH} \tag{22}$$

$$C_{eL}<C_{eH}<C_{vH}. \tag{23}$$

As shown in Fig. 4, there are two separate capacitance tuning ranges. To obtain one wider tuning range, we make the two ranges overlap partially, i.e.:

$$C_{vL}<C_{eH}=\frac{C_{vH}C_p}{C_{vH}+C_p}. \tag{24}$$

If the conditions can be met:

$$C_{vL}=\frac{C_{vH}C_p}{C_{vH}+C_p} \tag{25}$$

the widest tuning bandwidth is obtained at this point.

D. Design Flow With the Proposed Method

The inverse design process from the desired performances to the geometric parameters of the unit is shown in Fig. 5. Before the beginning, the lumped elements need to be selected according to the guidelines summarized above, while following the principle that the higher the desired transmission band, the smaller the capacitance of the lumped elements. Then, we can confirm the range of C_v and the parasitic parameters of R_v and L_v.

First, the lower limit C_{vL} of the varactor capacitance is taken as C_v and the upper limit f_H of the desired tuning range is taken as f_p into (9). Once we have a prescribed frequency zero f_z and passband bandwidth Δf, we can solve for C_1, L_1, and L_2 by the joint (9) – (11).

Here, we can check f_L by bringing C_{vH} into (9), Or the *RBW* by bringing α into (14). Also, we can check if the IL meets the design requirements by bringing in R_v. Note that no matter what the embedded elements are, the performances can be checked by simply introducing the equivalent lumped parameters.

Secondly, using the classical structure as the initial structure, we can obtain the initial geometric and the corresponding initial ECM parameters (C_1, L_1, L_2) of the unit, especially the relationship between them.

Then, we improve the unit structure based on the relationship between the geometric and ECM parameters, guided by the desired ECM parameters. The actual transmission performance of the designed unit can be obtained.

Finally, with the particle swarm optimization (PSO)-based curve-fitting method, we optimize and fit between the actual and desired performances to finally obtain the optimized geometric and ECM parameters.

Following, a paradigm based on the proposed design method and guidelines are provided.

III. Case Verification

A. RFSS Unit Design

We have known that for RFSS with varactors, the following approaches can be applied to realize the reduction of passband IL [30]:

1) Reduce R_v of the lumped elements.
2) Reduce the C_1 or the C_v (C_e).
3) Reduce L_1.
4) Increase L_2.

The R_v is determined by the processing technology of active elements. We can select active elements with smaller package resistance within a reasonable range. From the ECM method,

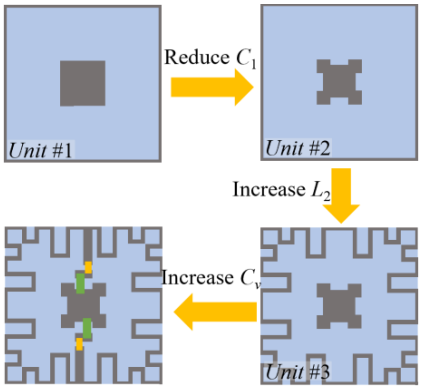

Fig. 6. The design process of the proposed RFSS unit.

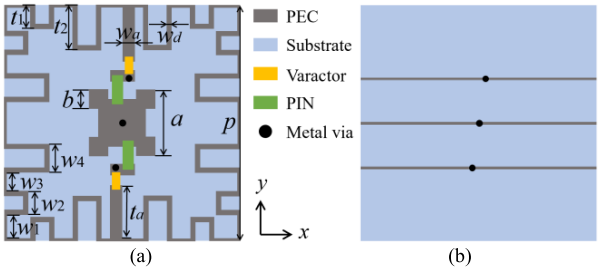

Fig. 7. The proposed RFSS unit. (a) Top layer and (b) Bias network on the bottom layer.

TABLE I
GEOMETRIC PARAMETERS OF THE PROPOSED RFSS UNIT

Parameter	Value (mm)	Parameter	Value (mm)	Parameter	Value (mm)
p	10	w_d	0.2	w_4	1.2
a	2.6	w_1	1	t_1	1
b	0.8	w_2	1	t_2	1.9
w_a	0.5	w_3	0.8	t_a	2.3

C_1 and L_1 are related to the unit period p and center patch size. We need to find the optimal values of C_1 and L_1 by taking into account the solder patch of the active elements, the bandwidth of the passband, the higher-order passbands, etc. In addition, L_2 is related to the grid around the perimeter, which can be reduced by convoluting the grid [40], [41].

The unit design process is shown in Fig. 6. First, we adopt the classical square slot as the initial structure of the unit, i.e., *Unit* #1 in Fig. 6. For the classical FSS structure, the fitting equations between the geometric parameters and the equivalent circuit parameters have been investigated by researchers. Therefore, we can obtain a set of parameters and take this set as the initial parameters.

For a wide tuning range of the transmission performance, we optimize the equivalent circuit parameters to achieve the desired transmission performance. Further, the unit structure needs to be improved to realize the desired equivalent circuit parameters.

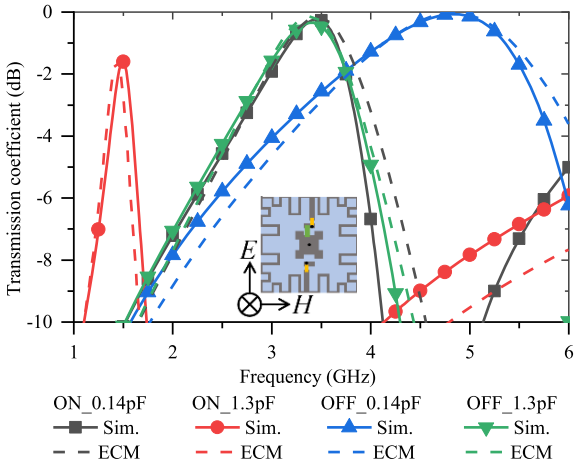

Fig. 8. The transmission coefficient curves simulated by CST simulation and calculated by ECM methods of the proposed RFSS unit with the PINs in different states and the varactors in different capacitance values.

C_1 is related to the equivalent capacitor of the inner square patch. We trim the center square patch of *Unit* #1 to reduce C_1 and obtain *Unit* #2. Then, we increase L_2 by convoluting the surrounding grids to obtain *Unit* #3. It reduces the IL without affecting the passband range because L_2 has a negligible effect on the passband tunable range and is inversely proportional to the IL at the passband. Moreover, embedding the PIN diode and varactor in a series relationship between the grid and the patch in *Unit* #3 results in a wider passband tunable bandwidth.

Finally, an RFSS unit with a wide passband tuning range and high transmittance is proposed in Fig. 7. The relationship between the equivalent circuit parameters and the geometric parameters of the anisotropic structure cannot be obtained directly. Here, we introduce the PSO-based curve-fitting method to obtain the corrected geometric parameters. The fitness of the geometric parameters can be evaluated by:

$$Fit=\sqrt{\frac{1}{N}\sum\left(\left|T^{SIM}\left(f_i\right)\right|-\left|T^{CAL}\left(f_i\right)\right|\right)^2} \tag{26}$$

where Fit is the fitness value, N is the number of frequency points taken into consideration, and T^{SIM} and T^{CAL} are the transmission coefficients based on simulated results from geometric parameters and the calculated ones by the ECM method at f_i, respectively. Through iteration and optimization, the geometric parameters of the RFSS are obtained in Table I, and the ECM parameters of the proposed element: L_1 = 2.812 nH, C_1 = 0.067 pF, L_2 = 5.120 nH.

The proposed RFSS unit consists of a convoluted grid around the perimeter, a trimmed center patch, and a set of varactors and PIN diodes. There are three metal vias connecting the top layer and three bias feeders on the bottom layer for the power supply of active elements. In order to reduce the effect of feeder networks on the performance of the proposed unit, a single-polarization RFSS unit is adopted here. The horizontal bias lines have a negligible effect on the *y*-polarized incident wave. Active elements are not placed along the centerline of the

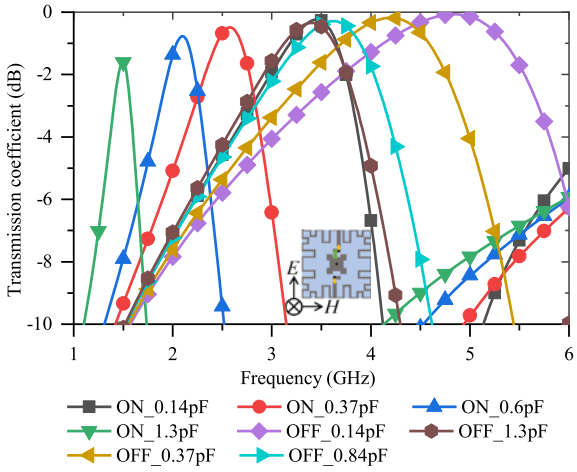

Fig. 9. The continuously tunable capacity of the proposed RFSS unit.

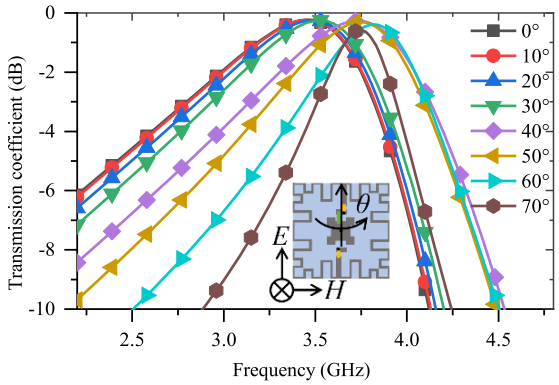

Fig. 10. The transmission coefficients of the proposed RFSS for different angles of incidence, in which the PINs are in the ON state and the C_v of the varactors are 0.14 pF.

configuration because of the need to balance the unit geometric parameters and the active element package dimension.

From the analysis in Section II, we adopt MA46H120 from MACOM as varactor [42], [43] and SMPA1320-079LF from SKYWORKS as PIN diode [44] to obtain a high capacitance tuning range α, a small parasitic resistor R_v and R_p, and a small lower capacitance limit C_{vL}. The adjustable parameters of the active elements are controlled by the applied bias voltage.

The dielectric slab we adopt here is F4B with the relative dielectric permittivity of ε_r = 2.45, the loss tangent of tanδ = 0.0014, and the thickness of h = 0.508 mm. The copper conductivity value σ is 59.6 × 10^6 S/m.

B. Performances and Analysis

To verify the transmission performances of the proposed RFSS, a full-wave simulation based on CST Microwave Studio is utilized.

The transmission characteristics of the proposed RFSS unit obtained by full-wave simulation and ECM calculation are present in Fig. 8. The *y*-polarized wave is normal incidence on

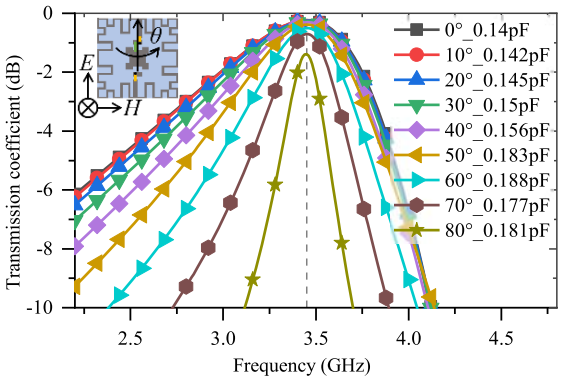

Fig. 11. The transmission coefficients of the proposed RFSS for different angles of incidence and different C_v of the varactors, in which the PINs are in the ON state.

the proposed infinite period surface. The simulated transmission coefficients are in good agreement with the calculated results based on the ECM method.

Fig. 9 exhibits the continuous passband tunable capacity of the proposed unit. When PINs are in the ON state, the transmission passband shifts from 1.49 GHz to 3.45 GHz as the varactor capacitance C_v changes from 1.3 pF to 0.14 pF. When PINs are in the OFF state, the transmission passband can be shifted from 3.40 GHz to 4.85 GHz as the C_v changes. In conclusion, the proposed RFSS enables tunable transmission passband from 1.49 to 4.85 GHz by switching the state of the PINs, while the IL obtains a minimum of 0.07 dB at 4.85 GHz and a maximum of 1.60 dB at 1.49 GHz. The total tunable RBW is 106.0%. The tunable transmission passband maintains high transmittance (IL < 1dB) over a wide range. The -1dB passband tunable range is from 1.82 to 5.36 GHz (with an RBW of 98.6%).

The most significant advantage of RFSS lies in its post-fabricated flexibility. We can regulate the active elements to achieve great performances at large angles of incidence. Taking the PINs in the ON state, the varactors at 0.14 pF, and the transmission passband resonance at 3.45 GHz as an example, we verified the angular stability of the proposed RFSS unit.

According to (1) – (3), the parameters of the substrate and the equivalent circuit change with the angle of incidence, which results in a deviation in the resonant frequency. Also, according to (9), the resonant frequency f_p is affected by the capacitance C_v. Therefore, the frequency shift introduced by the incidence angle can be compensated by adjusting the varactor capacitance C_v.

From Fig. 10, the resonant frequency varies with the angle of incidence. The frequency deviation occurs when the unit is irradiated by an incidence wave at an angle of over 40°. Meanwhile, there is a slight decrease in IL. From Fig. 11, the proposed RFSS unit can maintain the transmission passband constant at 3.45 GHz by controlling the capacitance value of the varactors under different incident angles wave irradiation. In addition, the loss of transmittance is acceptable. We conclude

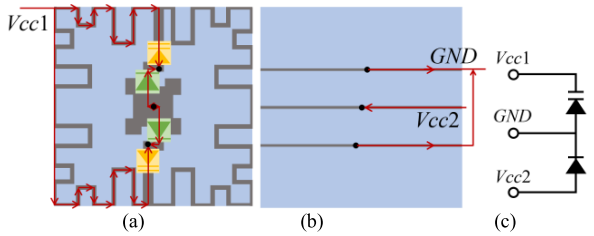

Fig. 12. The bias network configuration and direct current (dc) distribution of (a) The top layer and (b) The bottom layer of the proposed unit. (c) The equivalent circuit of the DC bias network.

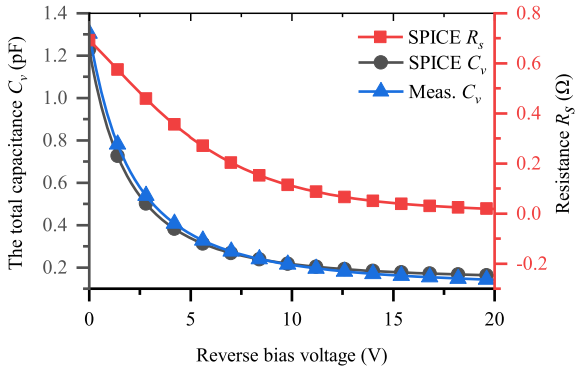

Fig. 13. The parasitic resistance R_v and capacitance C_v with reverse bias voltage $Vcc1$.

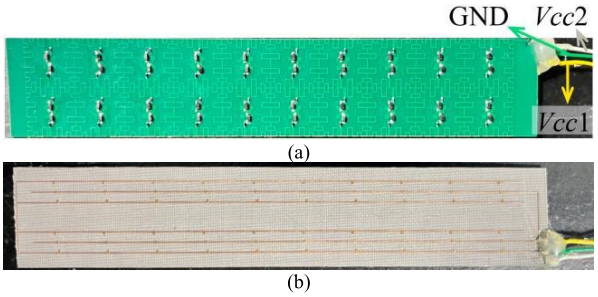

Fig. 14. The fabricated prototype. (a) Top layer and (b) Bottom layer.

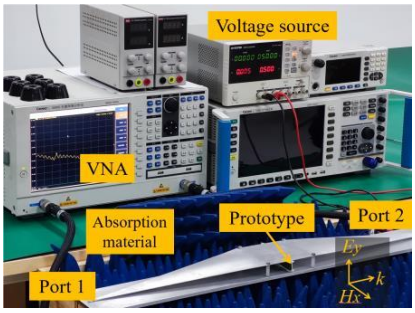

Fig. 15. The parallel plate waveguide measurement system.

that other cases will offer a similar performance level to the presented ones. That is, the proposed RFSS unit can maintain the stability of the resonance frequency and IL in the case of y-polarized wave incidence up to 70° by tunability.

IV. Fabrication and Experiment

A. Operating Mechanism

The bias network configuration and the direct current (dc) distribution at the top and bottom layer are shown in Fig. 12. The metal via hole at the connection between the PIN diode and the varactor diode is used for grounding (*GND*). The grid around the RFSS unit is used as the positive feeder of dc for the varactor, i.e., $Vcc1$ (varactors require reverse voltage supply). The metal via the hole in the center of the unit is used as the positive feeder of dc for the PIN diode, that is, $Vcc2$. All the active elements are in a parallel relationship.

For the varactor, the characteristics of parasitic resistance R_v and capacitance C_v with reverse bias voltage simulated by the SPICE model are shown in Fig. 13. However, for a more approximate prediction, there is a nonlinear junction capacitance equation for the measured varactor capacitance C_v [45]:

$$C_v\left(Vcc1\right) = C_j Vcc1 + C_{par} = \frac{C_{j0}}{\left(1 - Vcc1/V_j\right)^M} + C_{par} \quad (27)$$

where C_{j0} is the zero-bias junction capacitance, V_j is the built-in potential, $Vcc1$ is the applied revise voltage, M is the related doping-grading coefficient, and C_{par} is the parasitic capacitance. For MA46H120, better fitting parameters can be obtained by measurement [46]. There are: R_v = 2 Ω, L_v = 0.05 nH, C_{j0} = 1.2 pF, V_j = 4.155 V, M = 1.97, and C_{par} = 0.1044 pF. the parameters of the active elements are: R_v = 2 Ω, L_v = 0.05 nH, C_v = 0.14 – 1.3 pF, R_p = 0.47 Ω, L_p = 0.7 nH, C_p = 0.34 pF.

When the PIN diodes are in the OFF state, the $Vcc2$ does not supply. By supplying a voltage varying from 0 to 12 V to $Vcc1$, the capacitance of the varactor C_v can be varied to achieve tuning of the transmission passband in the high-frequency band. When the PIN diodes are in the ON state, the $Vcc2$ is supplied with a voltage of 0.95 V. $Vcc1$ is supplied with a series of voltages of 0 to 12 V to tune the transmission passband in the lower frequency band.

B. Fabricated and Measurement

A prototype consisting of 2 × 10 units was fabricated to measure and verify the reliability of the proposed design, as shown in Fig. 14. The prototype integrates the three dc feeders, and the feeders are connected externally at the edges (as green, yellow, and white line in Fig. 14).

The parallel plate waveguide (PPW) measurement system is set and shown in Fig. 15, which consists of a parallel plate waveguide, a vector network analyzer (VNA), a dc power supply source, and the absorption material side-placed. The measurement system obtains the transmission coefficient of the prototype by the comparison method. The TEM mode in the middle of the parallel plate waveguide along the y-polarization is used as the excitation source for the proposed unit. In addition, a free-space measurement is set up for the oblique incidence, as shown in Fig. 16. The oblique incidence is

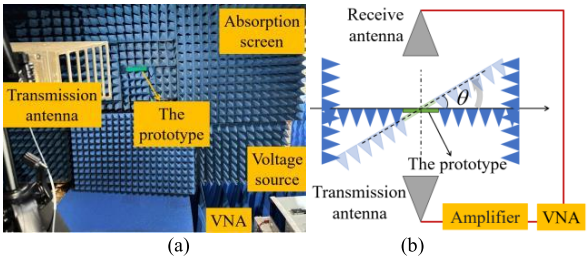

Fig. 16. The free-space measurement for the oblique incidence. (a) The measurement environment and (b) The system components.

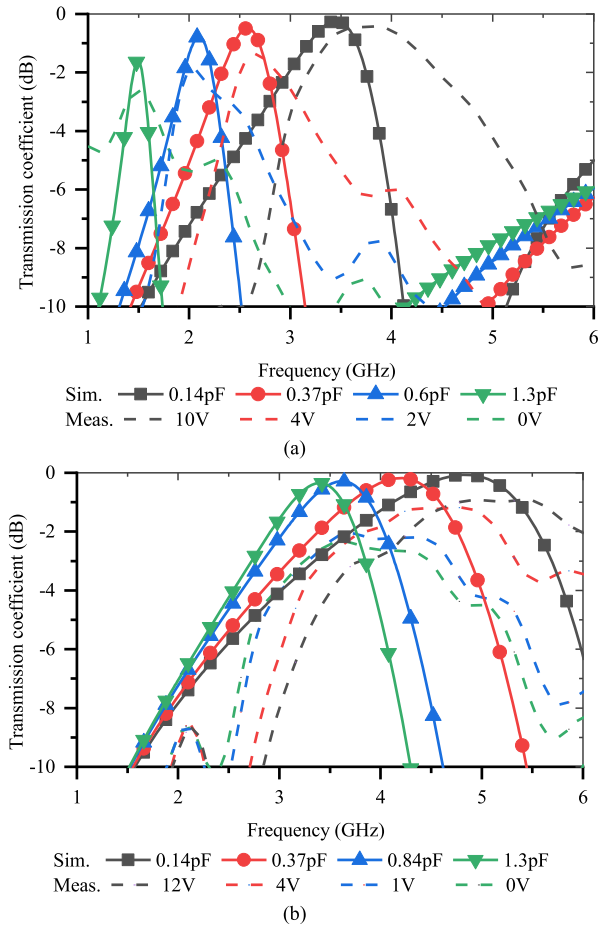

Fig. 17. The measured transmission coefficients of the proposed RFSS unit with varactors supplied with different voltages. (a) The PINs are in the ON state and (b) The OFF state.

realized by rotating the absorption screen. Prototypes that are not large enough for the free-space method may experience some degree of frequency deviation and very slight transmittance loss. The free-space measurement of the 2 × 10 units prototype is used only to verify the ability to achieve resonant frequency stabilization with tuning at oblique incidence of the prototype.

The measured results are exhibited in Figs. 17 – 21. The two dc channels are fed with different voltages to realize the tuning

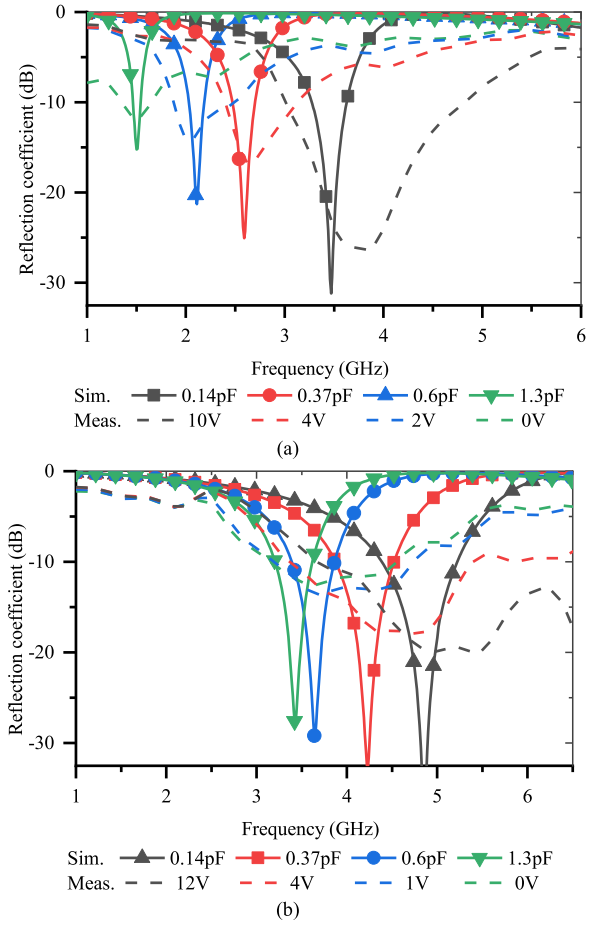

Fig. 18. The measured reflection coefficients of the proposed RFSS unit with varactors supplied with different voltages. (a) The PINs are in the ON state and (b) The OFF state.

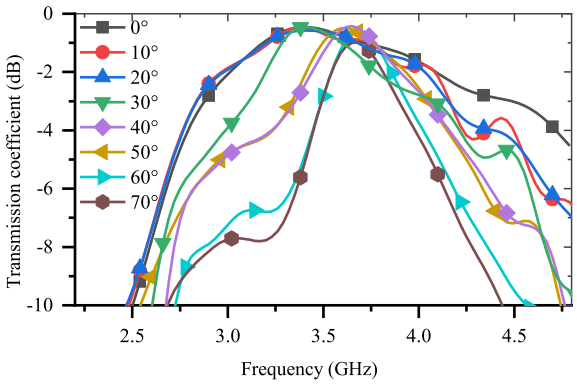

Fig. 19. The measured transmission coefficients of the proposed RFSS for different angles of incidence, in which $Vcc1$ = 8.5 V, $Vcc2$ = 0.95 V.

of the passband. From Fig. 17(a), when the PINs are in the OFF state ($Vcc2$ = 0 V), with the change of $Vcc1$ supply voltage (from 0 to 12V), the transmission passband can be tuned from 3.61 to 4.96 GHz with the IL ranges between 0.93 and 2.33 dB. From Fig. 17(b), when the PINs are in the ON state ($Vcc2$ =

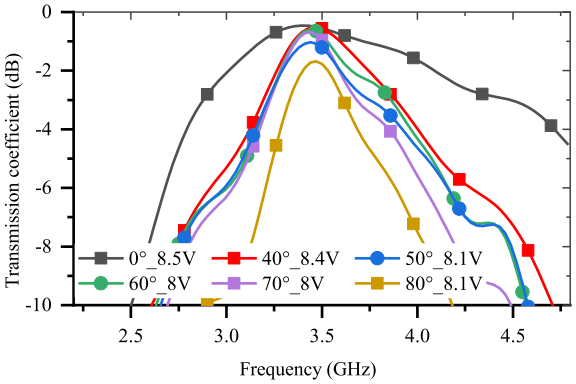

Fig. 20. The measured transmission coefficients of the proposed RFSS for different angles of incidence and different *Vcc*1, in which the *Vcc*2 = 0.95V.

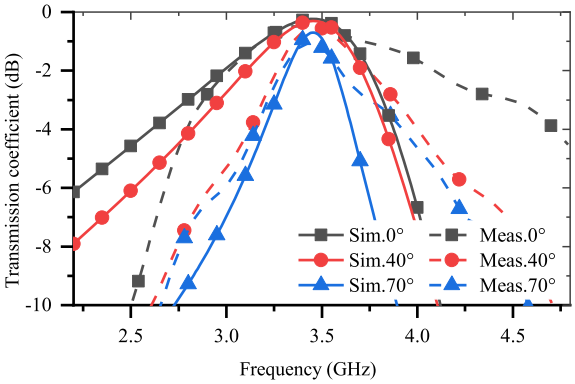

Fig. 21. The simulated and measured transmission coefficients of the proposed RFSS under different angles of incident wave irradiation with passband stabilized at 3.45 GHz.

0.95 V), the transmission passband can be tuned from 1.51 to 3.84 GHz with the IL ranges between 0.35 and 2.55 dB. Fig. 18 illustrates the reflection coefficients for the corresponding states.

From Fig. 19, the transmission coefficients of the proposed RFSS unit are shifted toward higher frequencies as the incident angle increases. At the same time, the passband bandwidth becomes narrower. This is in good agreement with the simulation results.

The frequency deviation of the proposed RFSS unit due to oblique incidence can be compensated by the adjustable varactor, thus maintaining angular stability at large angles, as shown in Fig. 20. The measured and simulated transmission coefficients of the proposed RFSS unit with passband stabilized at 3.45 GHz are shown in Fig. 21 for angles of incidence of 0°, 40°, and 70°, respectively. The proposed unit can maintain the stability of resonant frequencies and the IL through reconfigurability.

To facilitate the comparison of simulation and measured results, Fig. 22 illustrates the variation of the resonant frequencies f_p and IL with the angle of incidence, in which the simulation conditions are: PINs in the ON state and C_v adjusted

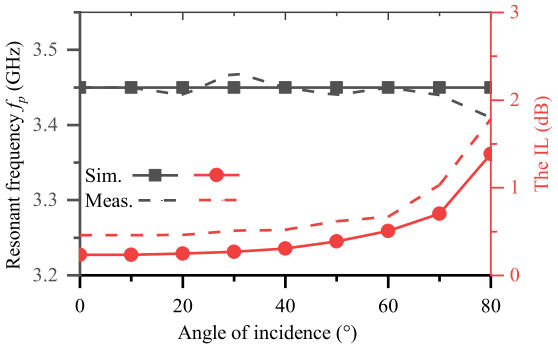

Fig. 22. The curves of resonant frequency f_p and the IL as a function of the incident angle of the proposed RFSS unit, in which the PINs are in the ON state (*Vcc*2 = 0.95 V) and the C_v (*Vcc*1) are adjusted with the incident angle.

with the incident angle, and the measurement conditions are: *Vcc*2 = 0.95 V and the *Vcc*1 is adjusted with the incident angle. We can evaluate the stability of the resonance frequency with respect to the angle of incidence by the frequency deviation ration R_{fd}:

$$R_{fd} = \frac{Max\left(\left|f_{p\_\theta_i} - f_{p\_0^\circ}\right|\right)}{f_{p\_0^\circ}} \times 100\% \quad (28)$$

Theoretically, the proposed unit can be tuned to achieve $R_{fd} = 0$, as shown in the simulated results in Fig. 22. From Fig. 22, the resonate frequency is in agreement with the simulation results, and the $R_{fd} = 0.58\%$ for the measurement results. The R_{fd} of the measured results can be improved by decreasing the minimum step of the dc supply voltage and increasing the sampling rate of the VNA. The IL of the prototype follows the same trend as the simulated one but is slightly larger. This may be due to parameter fluctuations of lumped elements and measurement errors in small-sized prototype.

C. *Discussion and Comparison*

In conclusion, the proposed RFSS unit can provide a series of highly efficient transmission passbands from 1.51 to 4.96 GHz with IL ranging from 0.35 to 2.55 dB. In the case of oblique incidence, good angular stability up to 70° can be maintained by the reconfigurable properties. Compared with the simulated results, the resonance passband is biased towards higher frequencies and the IL increases slightly, which may be due to the manufacturing inaccuracy, measurement tolerance, and the soldering and parameter fluctuations of the active elements under microwave band applications. The discrepancy in the passband bandwidth of the proposed RFSS unit in terms of its agreement with the simulation results can be attributed to the difference between the extracted parameters of the lumped elements (varactor and PIN diode) and the values used for the simulation. Embedded element parameter calibration is critical to the accuracy of RFSS designs.

We have presented the comparison of this work and the existing state-of-the-art in Table II. Compared with the works that are embedded with varactors, this work has the widest passband tunable range, the best optimum value of the IL, and

TABLE II
THE COMPARISON OF THIS WORK WITH OTHER SIMILAR WORKS

Refs.	Transmission passband (GHz)	Tunable RBW	Meas. IL (dB)	3-dB bandwidth of passband[&] (GHz)		Varactor	Capacitance tuning		Package resistance (Ω)	Incidence angle variation and R_{fd}[&]
				@ f_L	@ f_H		range (pF)	ratio α		
[26]	1.4 – 2.75	65%	1.0 – 4.5	None	2.58 – 2.87 (10.6%)	SMV1405 -040LF	0.56 – 2.8	5	0.8	60°, 9.04%
[27]	3.7 – 5.2	33.7%	3 – 6	None	4.97 – 5.22 (4.9%)	MA46H120	0.12 – 0.38	3.17	2	60°, 2.04%
[29]	3.76 – 4.25	12.2%	0.98 – 1.97	3.75 – 3.97 (5.7%)	4.07 – 4.55 (11.1%)	SMV2201 -040LF	0.23 – 0.34	1.48	N.A.	30°, 0.93%
[30]	4.84 –5.9	19.7%	0.51 – 1.09	4.28 – 5.4 (23.1%)	5.05 – 7.03 (32.8%)	MA46H120	0.14 – 0.34	2.43	2	45°, 1.35%
[31]	3.62 – 4.25	16%	0.72 – 1.71[&]	3.41 – 3.92 (13.9%)	3.61 – 4.6 (24.1%)	SMV2020 -079LF	0.35 – 3.2	9.1	2.5	45°, 0.24%
[32]	2.8 – 4.9	84.5%	N.A.	N.A.	N.A.	MA46H120	0.14 – 1.3	9.3	2	75°, 1.37%
[33]	1.14 – 1.35 / 2.01 – 2.61	16.9% / 26%	1.43 – 3.65[&]	None	2.51 – 2.68 (6.6%)	BBY53 / BB857	0.52 – 1 / 1.8 – 3	1.92 / 1.67	0.47 / 1.5	60°, 1.03%
[35]	3.4 – 6.4	61.2%	0.7 – 6.3	None	5.65 – 7.1 (22.7%)	MA46H120	0.2 – 1.3	6.5	2	45°, 0.43%
This work	1.51 – 4.96	106.6%	0.35 – 2.55	1.41 – 1.61 (13.2%)	3.63 – 6.22 (52.6%)	MA46H120	0.1* – 1.3	13	2 / 2.47[#]	70°, 0.58%

*: The lower limit of the capacitance tuning range C_{eL} of this work is calculated according to (22).
#: The package resistance of the proposed work varies with the state. When the PIN is in the OFF state, the package resistance is that of the varactor. When the PIN is in the ON state, the package resistance is the varactor in series with the PIN.
&: Estimated values from paper. N.A.: Not available from paper.
None: The IL at the lowest frequency exceeds 3 dB resulting in an inability to evaluate the bandwidth.

the largest angular stability. Since it is difficult for RFSS to take into account the change in passband bandwidth under angular variation, here, angular stability is mainly concerned with the variation of the resonance frequency and IL with the angle of incidence. It is necessary to point out that the angular stability performance of the Ref. [31] and this work relies on the modulation of the tunability. Compared to the works with wide tunable bandwidths [32], [35], this work has significant advantages in terms of IL in addition to the tunable bandwidth. Compared to the works that also adopt the MA46H120 [27], [30], [32], [35] the proposed work widens the lower limit of the capacitance, fully utilizes the tunable range of the varactor, and achieves the widest tunable RBW. At low frequencies, the proposed work has a reasonable level of passband bandwidth compared to other similar works. At high frequencies, the passband bandwidth inevitably increases because of the small IL.

By selecting the appropriate elements and connecting them in series into the switchable PIN diodes, the capacitance tuning range is widened, and then the widest transmission passband tuning range is realized. Moreover, the IL of the proposed work is significantly lower. The good measurement performance of the proposed RFSS unit verifies the feasibility of the proposed design guidelines for transmission passband tunable RFSS with embedded varactor.

V. CONCLUSION

In this paper, we propose a systematic and effective design method to reduce the complexity and difficulty of high-performance tunable RFSS with varactor. Moreover, the guidelines for broadening the tunable RFSS are presented. The feasibility and validity are verified with a fabricated and measured paradigm. Relying on the great post-processing flexibility, the proposed prototype achieves a tunable transmission passband RBW of 106.6% and an IL of no more than 2.55 dB. Moreover, it can maintain good stability of resonance frequencies and IL as the angle of incidence varies from 0° to 70° through tuning. As evidenced by the performance of the proposed RFSS, the design method and guidelines proposed in this paper show attractive potential applications for stealth technology and efficient communication.

REFERENCES

[1] T. K. Wu, Ed., *Frequency Selective Surface and Grid Array*. New York, NY, USA: Wiley, 1995.
[2] B. A. Munk, *Frequency Selective Surfaces: Theory and Design*. New York, NY, USA: Wiley, 2000.
[3] A. A. Omar and Z. Shen, "Thin bandstop frequency-selective structures based on loop resonator," *IEEE Trans. Microw. Theory Techn.*, vol. 65, no. 7, pp. 2298–2309, July 2017.
[4] S. Ghosh and S. Lim, "Fluidically reconfigurable multifunctional frequency-selective surface with miniaturization characteristic," *IEEE Trans. Microw. Theory Techn.*, vol. 66, no. 8, pp. 3857–3865, Aug. 2018.
[5] Z. Xue, S. Zhong, and Y. Ma, "Graphene-FSS hybrid absorptive structure with amplitude/frequency dual-modulated passband," *IEEE Trans. Microw. Theory Techn.*, vol. 20, no. 9, pp. 1711–1715, Sept. 2021.
[6] M. Safari, C. Shafai, and L. Shafai, "X-band tunable frequency selective surface using MEMS capacitive loads," *IEEE Trans. Antennas Propag.*, vol. 63, no. 3, pp. 1014–1021, March 2015.
[7] S. A. Nauroze and M. M. Tentzeris, "A thermally actuated fully inkjet-printed origami-inspired multilayer frequency selective surface with continuous-range tunability using polyester-based substrates," *IEEE*

Trans. Microw. Theory Techn., vol. 67, no. 12, pp. 4944–4954, Dec. 2019.

[8] F. Erkmen, T. S. Almoneef, and O. M. Ramahi, "Scalable electromagnetic energy harvesting using frequency-selective surfaces," *IEEE Trans. Microw. Theory Techn.*, vol. 66, no. 5, pp. 2433–2441, May 2018.

[9] L. Liu, H. Zhai, D. Hu, and S. Ren. "A polarization-stable frequency selective rasorber with miniaturized elements and wideband absorbing properties," *Microw. Opt. Techn. Lett.*, vol. 62, no. 4, pp. 1643–1650, 2020.

[10] Y. Ding et al., "Ultrawideband frequency-selective absorber designed with an adjustable and highly selective notch," *IEEE Trans. Antennas Propag.*, vol. 69, no. 3, pp. 1493–1504, March 2021.

[11] F. Erkmen and O. M. Ramahi, "A scalable, dual-band absorber surface for electromagnetic energy harvesting and wireless power transfer," *IEEE Trans. Antennas Propag.*, vol. 69, no. 10, pp. 6982–6987, Oct. 2021.

[12] W. Gong et al., "A low-profile energy selective surface with ultra-wide absorption band," *IEEE Trans. Microw. Theory Techn.*, vol. 71, no. 3, pp. 1348–1355, March 2023.

[13] F. Bayatpur and K. Sarabandi, "A tunable metamaterial frequency-selective surface with variable modes of operation," *IEEE Trans. Microw. Theory Techn.*, vol. 57, no. 6, pp. 1433–1438, June 2009.

[14] Q. Chen et al., "Thin and broadband electromagnetic absorber design using resistors and capacitors loaded frequency selective surface," *J. Electromagn. Waves Appl.*, vol. 26, no. 16, pp. 2102–2111, 2012.

[15] A. Sharma, S. Malik, S. Ghosh, and K. V. Srivastava, "A miniaturized frequency selective rasorber with independently regulated selective dual-transmission response," *IEEE Antennas Wireless Propag. Lett.*, vol. 21, no. 2, pp. 257–261, Feb. 2022.

[16] Z. Huang et al., "Partition layout loading of frequency selective surface absorbers on the curved surfaces for the significant RCS reduction," *IEEE Trans. Microw. Theory Techn.*, vol. 70, no. 6, pp. 2948–2954, June 2022.

[17] C. Huang, J. Song, C. Ji, J. Yang, and X. Luo, "Simultaneous control of absorbing frequency and amplitude using graphene capacitor and active frequency-selective surface," *IEEE Trans. Antennas Propag.*, vol. 69, no. 3, pp. 1793–1798, March 2021.

[18] F. Bayatpur and K. Sarabandi, "Tuning performance of metamaterial-based frequency selective surfaces," *IEEE Trans. Antennas Propag.*, vol. 57, no. 2, pp. 590–592, Feb. 2009.

[19] D. S. Wang, P. Zhao, and C. H. Chan, "Design and analysis of a high-selectivity frequency-selective surface at 60 GHz," *IEEE Trans. Microw. Theory Techn.*, vol. 64, no. 6, pp. 1694–1703, June 2016.

[20] P. Rodríguez-Ulibarri, M. Navarro-Cía, R. Rodríguez-Berral, F. Mesa, F. Medina, and M. Beruete, "Annular apertures in metallic screens as extraordinary transmission and frequency selective surface structures," *IEEE Trans. Microw. Theory Techn.*, vol. 65, no. 12, pp. 4933–4946, Dec. 2017.

[21] S. C. Bakshi, D. Mitra, and F. L. Teixeira, "Wide-angle broadband rasorber for switchable and conformal application," *IEEE Trans. Microw. Theory Techn.*, vol. 69, no. 2, pp. 1205–1216, Feb. 2021.

[22] H. Jiang, S. Liao, R. Li, and Q. Xue, "Independently switchable rasorber with wide transmission and low-reflection bands under dual polarization," *IEEE Trans. Microw. Theory Techn.*, vol. 72, no. 2, pp. 863–877, Feb. 2024.

[23] Y. Ma et al., "Broadband RCS reduction metasurface with a reconfigurable high-selectivity transmission band," *IEEE Trans. Microw. Theory Techn.*, vol. 72, no. 2, pp. 878–891, Feb. 2024.

[24] C. Mias, "Varactor-tunable frequency selective surface with resistive-lumped-element biasing grids," *IEEE Microw. Wireless Compon. Lett*., vol. 15, no. 9, pp. 570–572, Sept. 2005.

[25] F. Bayatpur and K. Sarabandi, "Design and analysis of a tunable miniaturized-element frequency-selective surface without bias network," *IEEE Trans. Antennas Propag.*, vol. 58, no. 4, pp. 1214–1219, April 2010.

[26] X. G. Huang, Z. Shen, Q. Y. Feng, and B. Li. "Tunable 3-D bandpass frequency-selective structure with wide tuning range," *IEEE Trans. Antennas Propag.*, vol. 63, no. 7, pp. 3297–3301, July 2015.

[27] A. Ebrahimi, Z. Shen, W. Withayachumnankul, S. F. AI-Sarawi, and D.Abbott, "Varactor-tunable second-order bandpass frequency-selective surface with embedded bias network," *IEEE Trans. Antennas Propag.*, vol. 64, no. 5, pp. 1672–1680, May 2016.

[28] S. Ghosh and K. V. Srivastava, "A dual-band tunable frequency selective surface with independent wideband tuning," *IEEE Antennas Wireless Propag. Lett.*, vol. 19, no. 10, pp. 1808–1812, Oct. 2020.

[29] S. C. Bakshi, D. Mitra, and F. L. Teixeira, "Multifunctional frequency selective rasorber with dual mode and continuous tunability," *IEEE Trans. Antennas Propag.*, vol. 69, no. 9, pp. 5704–5715, Sept. 2021.

[30] M. Guo et al., "Analysis and design of a high-transmittance performance for varactor-tunable frequency-selective surface," *IEEE Trans. Antennas Propag.*, vol. 69, no. 8, pp. 4623–4632, Aug. 2021.

[31] H. Bai et al., "Tunable frequency selective surface with angular stability," *IEEE Antennas Wireless Propag. Lett.*, vol. 20, no. 6, pp. 1108–1112, June 2021.

[32] D. Zhai, X. Huang, Y. Xu, and P. Liu, "A design of thin-layer frequency selective surface with wideband tunability and incidence stability," *2022 IEEE 9th Int. Symp. Microw., Antenna, Propag. and EMC Techn. Wireless Commun. (MAPE)*, Chengdu, China, pp. 306–309, 2022.

[33] Y. -H. Ma, D. -W. Wang, Y. Yu, and W. -S. Zhao, "Design of dual-band frequency-selective surfaces with independent tunability," *IEEE Trans. Antennas Propag.*, vol. 70, no. 12, pp. 12381–12386, Dec. 2022.

[34] B. Jiang, H. Hu, J. Tian, S. Lei, M. Chen, and B. Chen, "A polarization-insensitive dual-band FSS with high selectivity and independently switchable characteristics," *IEEE Antennas Wireless Propag. Lett.*, vol. 22, no. 1, pp. 14–18, Jan. 2023.

[35] L. -M. Zhang, X. Ding, and W. Shao, "A multifunctional active frequency selective surface with scattering diffusivity and transmission passband tunability," *IEEE Antennas Wireless Propag. Lett.*, vol. 23, no. 1, pp. 229–233, Jan. 2024.

[36] R. J. Langley, E. A. Parker, "Double-square frequency-selective surfaces and their equivalent circuit," *Electron. Lett.*, vol. 19, no. 17, pp. 675–677, 1983.

[37] I. Bahl, M. Bozzi, R. Garg, *Microstrip Lines and Slotlines*, *Third Edition*, Artech, 2013.

[38] G. L. Matthaei, L. Young, and E. M. T. Jones, *Microwave Filters, Impedance-Matching Networks, and Coupling Structures*. Norwood, MA, USA: Artech House, 1980.

[39] D. Ferreira, R. F. S. Caldeirinha, I. Cuiñas, and T. R. Fernandes, "Square loop and slot frequency selective surfaces study for equivalent circuit model optimization," *IEEE Trans. Antennas Propag.*, vol. 63, no. 9, pp. 3947–3955, Sept. 2015.

[40] C. Zhao, C.-F. Wang, and S. Aditya, "Power-dependent frequency-selective surface: concept, design, and experiment," *IEEE Trans. Antennas Propag.*, vol. 67, no. 5, pp. 3215–3220, May 2019.

[41] D. Ferreira, R. F. D. Caldeirinha, I. Cuiñas, and T. R. Fernandes, "Tunable square slot FSS EC modelling and optimisation," *IET Microw., Antennas Propag.*, vol. 43, no. 6, pp. 508–511, Oct. 2004.

[42] MACOM Technology Solutions, *MA46H120 Varactor Datasheet* [Online]. Available: https://cdn.macom.com/datasheets/MA46H120%20Series.pdf

[43] MACOM technology solutions, *MA46H120 Varactor SPICE* [Online]. Available: https://cdn.macom.com/files/MAVR-000120_MA46H120SPICE-ADS Model.pdf

[44] "SMP1320 series: Low resistance, low capacitance, plastic packaged PIN diodes," May 2017. [Online]. Available: http://www.alldatasheet.com/datasheet-pdf/pdf/201106/SKYWORKS/SMP1302.html

[45] Q. Chen, X. Chen, H. Cai, and F. Chen, "Schottky diode large-signal equivalent-circuit parameters extraction for high-efficiency microwave rectifying circuit design," *IEEE Trans. Circuits Syst. II Express Briefs*, vol. 67, no. 11, pp. 2722–2726, Nov. 2020.

[46] N. Nguyen-Trong, T. Kaufmann, L. Hall, and C. Fumeaux, "Analysis and design of a reconfigurable antenna based on half-mode substrate-integrated cavity," *IEEE Trans. Antennas Propag.*, vol. 63, no. 8, pp. 3345–3353, Aug. 2015.